





Formation of Fano line shapes in optical responses and spectra of internal fields of excitonic nanospheres

Shinji Hayashi ^{1,2,*}, Hiroshi Sugimoto ¹, Minoru Fujii ¹, Dmitry V. Nesterenko ^{3,4} and Zouheir Sekkat^{2,5}

¹*Department of Electrical and Electronic Engineering, Graduate School of Engineering, Kobe University, Kobe 657-8501, Japan*

²*Optics and Photonics Center, Moroccan Foundation for Science, Innovation and Research (MAScIR), University Mohammed VI Polytechnic, Ben Guerir 43150, Morocco*

³*Faculty of Information Technology, Samara National Research University, Samara 443086, Russia*

⁴*Diffractive Optics Laboratory, IPSI RAS - Branch of the FSRC "Crystallography and Photonics" RAS, Samara 443086, Russia*

⁵*Faculty of Sciences, Mohamed V University in Rabat, Rabat 10010, Morocco*



(Received 26 April 2023; revised 11 August 2023; accepted 21 August 2023; published 8 September 2023)

Dielectric nanoparticles not showing distinct Mie resonances have been discarded as useful elements of resonant nanophotonics. However, the incorporation of the excitonic transition into such nanoparticles may allow us to generate sharp resonances, in particular, Fano resonances, thereby enhancing the utility of such nanoparticles. In this work, on the basis of the Mie theory and its electrostatics approximation, we analyze analytically and numerically optical responses and resonant behaviors of internal fields in spherical excitonic nanoparticles. The excitonic sphere is characterized by a dielectric constant consisting of a background dielectric constant and a Lorentzian response of the exciton excitation. From equations of the electrostatics approximation, by appropriately accounting for the background scattering, it is shown analytically that the absorption efficiency is expressed as a Lorentzian function, while the efficiencies of the scattering and extinction are expressed in the form of the generalized Fano function (external Fano resonance). From the same procedures, it is also shown that the spectra of the enhancement factor of internal fields are described by the same generalized Fano function (internal Fano resonance). Equations appearing in the derivation clearly indicate that both the external and internal Fano resonances are caused by the interference between a nonresonant component and a resonant component, corresponding to a broad background and sharp excitonic transition, respectively. Assuming a model excitonic sphere that mimics a polymer sphere doped with J-aggregates of excitonic molecules, spectra of scattering, absorption and extinction efficiencies, as well as that of the enhancement factor of internal fields, are calculated including a size range beyond the small particle limit, for which the exact Mie theory is used. The generalized Fano functions are shown to reproduce very well the calculated spectra even beyond the small particle limit, provided that the sphere radius is less than an upper bound. The results of the present paper provide a firm basis for discussing the formation of the Fano line shapes in optical responses and spectra of internal fields of excitonic nanospheres.

DOI: [10.1103/PhysRevB.108.125408](https://doi.org/10.1103/PhysRevB.108.125408)

I. INTRODUCTION

Over the past decade, Fano resonances, characterized by asymmetric spectral line shapes, in a variety of nanostructures including metallic and dielectric nanoparticles, metamaterials and photonic crystals, have been the subject of intensive experimental and theoretical studies since they find potential applications in sensing, optical switching, enhanced spectroscopies, and so on [1–4]. The Fano line shapes exhibited by single nanoparticles, one of the simplest nanostructures, have been analyzed based on the theory of Mie scattering.

In 1908, Mie developed an electromagnetic theory that allows us to calculate cross sections of scattering, absorption, and the extinction of a single sphere of arbitrary size illuminated by an electromagnetic plane wave [5]. Even more than a century later, the Mie theory still provides a basis for discussing various optical properties resulting from Mie resonances associated with the excitation of electric and magnetic modes supported by nanoparticles [6–9].

Recent analyses based on the exact Mie theory showed that, in a metallic sphere which supports electric modes (plasmon modes), Fano line shapes are generated in forward and backward (directional) scattering due to the interference of scattered waves associated with a broad electric dipole mode and a sharp electric quadrupole mode [10,11]. On the other hand, in a high-index dielectric sphere, which supports both the electric and magnetic modes, the interference between scattered waves associated with a broad electric dipole mode and a sharp magnetic dipole mode was shown to generate the Fano line shapes in directional scattering [11]. Furthermore,

*s.hayashi@dragon.kobe-u.ac.jp

Tribelsky and Miroshnichenko [12] showed that a cascade of Fano resonances in total scattering can take place in a high-index dielectric sphere with a size parameter x (defined by $x = 2\pi\sqrt{\epsilon_m}R/\lambda$ with the radius of the sphere R , the dielectric constant of surrounding medium ϵ_m , and the wavelength of the incident light λ) falling in the range of $x \sim 1$, i.e., the range of Mie-tronics [13–15]. The Fano resonances in metal core-dielectric shell spheres have been observed experimentally for the ZnS-coated Au sphere by Chen *et al.* [16] and theoretically analyzed by Arruda *et al.* [17]. Jule *et al.* [18] analyzed theoretically the Fano resonances in a dielectric core-metal shell sphere much smaller than the wavelength of incident light. Very recently, Wang *et al.* [19] and Minin *et al.* [20] discovered high-order Fano resonances in a low-index dielectric sphere with x values falling in the range of $x \sim 10$, i.e., the range of mesotronics [21,22].

In recent years, particular attention has been paid to high-index dielectric nanoparticles that show pronounced Mie resonances in the visible region. The low-loss nanostructures are currently under intensive experimental and theoretical studies towards realizing highly efficient optical nanodevices based on the Mie resonances (Mie-tronics) [13–15], overcoming the problems of losses in plasmonic nanodevices. In contrast to the high-index dielectric nanoparticles, those having relatively low refractive indices did not attract much attention because they show only monotonous spectra without resonant peaks; when they are sufficiently small, they show scattering spectra obeying the $1/\lambda^4$ -law of Rayleigh scattering [6]. However, even for low-index dielectric nanoparticles, it is possible to generate sharp resonances, in particular, Fano resonances, if excitonic transitions are incorporated into them. The simplest way is to use the nanoparticles of excitonic materials. Halide perovskites are materials attracting great interest in recent years because of their strong exciton resonances at room temperature. Very recently, Muckel *et al.* [23] reported the experimental observation of the Fano line shape in dark field-scattering spectra of thin films consisting of nanograins of $(\text{C}_4\text{H}_9\text{NH}_3)_2\text{PbI}_4$. Since their samples showed broad background scattering, they concluded that the Fano resonance originated from the interference between the exciton resonance and the broad background scattering. In previous reports on similar halide perovskites nanoparticles, Tiguntseva *et al.* [24] suggested the coupling of the exciton resonance with the Mie resonance of the nanoparticle itself [24] as the origin of the Fano resonance, while Cai *et al.* [25] reported the Fano resonance arising from the coupling of the exciton resonance with plasmon resonances of Ag nanostructures. In contrast to these reports, the report of Muckel *et al.* [23] suggested that no distinct resonance was necessary and just a broad background scattering was sufficient to generate the Fano resonance through the coupling with the exciton resonance. This simple mechanism of the Fano resonance is expected to work not only in the halide perovskites nanoparticles, but also in a wide range of excitonic nanoparticles having relatively low background refractive indices, for instance, glass or polymer nanoparticles doped with J-aggregates of excitonic molecules. However, systematic studies of the Fano resonances generated by such a mechanism are still lacking, and influences of various sample parameters like the size of

nanoparticles and dielectric constant of surrounding medium on the Fano line shape are not yet well known.

In this work, on the basis of the Mie theory and its electrostatics (ES) approximation valid for a sufficiently small particle (small-particle limit), we perform systematically analytical and numerical studies of scattering, absorption, and extinction spectra of a spherical excitonic nanoparticle. We also extend our study to Fano-resonant behaviors of electric fields induced inside the sphere (internal fields). The present analytical and numerical results provide a firm basis for discussing the formation of Fano line shapes in scattering and extinction spectra as well as in the spectra of the internal fields. For both the optical spectra and the spectra of internal fields, we show that the Fano line shapes are generated by the interference between a resonant component associated with the exciton excitation and a nonresonant broad background. This paper is organized as follows. In Sec. II, line shapes of scattering, absorption, and extinction spectra of an excitonic sphere are investigated. First, we show analytically that, in the small-particle limit, the absorption spectrum is expressed as a Lorentzian function and the scattering and extinction spectra are expressed in the form of generalized Fano function. Second, from numerical calculations of the spectra for a model excitonic sphere performed by the exact Mie theory, we show that the Lorentzian and generalized Fano functions are still valid even beyond the small-particle limit, provided that the particle radius is smaller than an upper bound. In Sec. III, Fano-resonant behaviors of the internal fields are analyzed. It is shown that in the small-particle limit, the enhancement factor of the internal fields can be expressed by the same generalized Fano function as that of the scattering spectra, and the generalized Fano function remains valid even beyond the small-particle limit until an upper bound radius.

II. SPECTRA OF SCATTERING, ABSORPTION, AND EXTINCTION

A. Analytical analyses based on electrostatics approximation

1. Line-shape functions

Let us consider an excitonic sphere of radius R characterized by a dielectric function $\epsilon(\omega)$ placed in a surrounding medium with a dielectric constant ϵ_m , as schematically shown in Fig. 1. We use the following expression of the dielectric function resulting from the Lorentz oscillator model [6], which has been widely used for the discussion of optical properties of excitonic materials including the halide perovskites [23,26] and J-aggregates of dye molecules [27,28]:

$$\epsilon(\omega) = \epsilon_b - \frac{f\omega_{\text{exc}}^2}{\omega^2 - \omega_{\text{exc}}^2 + i\omega\gamma_{\text{exc}}}, \quad (1)$$

where ω_{exc} is the excitonic transition frequency, γ_{exc} the corresponding damping rate, f the oscillator strength, and ϵ_b the background dielectric constant. Normally, all the parameters entering in the above expression take real values. In general, an excitonic transition gives rise to a Lorentzian line in the absorption spectrum, which can be well described by the second term of $\epsilon(\omega)$.

As summarized in the Supplemental Material [29], the Mie theory [5,6] allows us to calculate efficiencies (cross

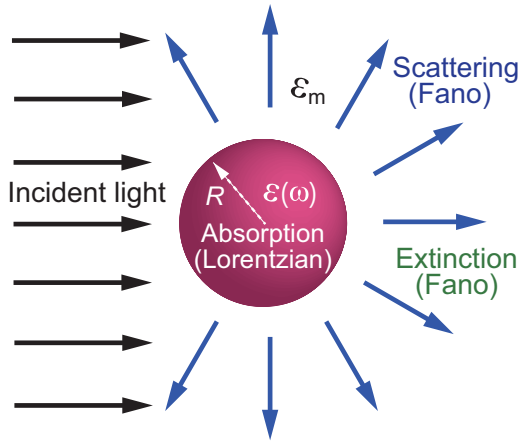


FIG. 1. Excitonic sphere illuminated by incident light.

sections normalized to the cross-sectional area πR^2) of scattering Q_{sca} , absorption Q_{abs} , and extinction Q_{exc} for a sphere with an arbitrary radius R . The efficiencies are expressed in terms of the Mie coefficients a_n and b_n , which correspond to the excitation of n th-order electric and magnetic modes of the sphere, such as the electric dipole, electric quadrupole, magnetic dipole, and magnetic quadrupole modes [6]. In the case of a sphere much smaller than the wavelength of incident light λ (small-particle limit), i.e., when the size parameter defined by $x = 2\pi R\sqrt{\epsilon_m}/\lambda$ is much less than unity, it is known that the optical response of the sphere is determined only by the lowest-order electric mode corresponding to a_1 . In this case, Q_{sca} and Q_{abs} reduce to simple expressions derived within the ES approximation [6]. From Eqs. (S7) and (S8) of the Supplemental Material [29], the efficiencies in the ES approximation can be written as

$$Q_{\text{sca}} = \frac{8}{3}x^4 \left| \frac{\epsilon(\omega) - \epsilon_m}{\epsilon(\omega) + 2\epsilon_m} \right|^2, \quad (2)$$

and

$$Q_{\text{abs}} = 4x \text{Im} \frac{\epsilon(\omega) - \epsilon_m}{\epsilon(\omega) + 2\epsilon_m}. \quad (3)$$

Furthermore, Q_{ext} is given by

$$Q_{\text{ext}} = Q_{\text{sca}} + Q_{\text{abs}}. \quad (4)$$

Using these expressions together with $\epsilon(\omega)$ given by Eq. (1), we first derive analytical expressions of line shape functions.

For convenience, we write the second term of $\epsilon(\omega)$ [Eq. (1)] responsible for the Lorentzian line shape as $fL(\omega)$, then we can write as $\epsilon(\omega) = \epsilon_b - fL(\omega)$. Inserting this expression into the factor common to Q_{sca} and Q_{abs} we can derive

$$\frac{\epsilon(\omega) - \epsilon_m}{\epsilon(\omega) + 2\epsilon_m} = \left(\frac{\epsilon_b - \epsilon_m}{\epsilon_b + 2\epsilon_m} \right) \chi(\omega), \quad (5)$$

with

$$\chi(\omega) = \frac{1 - c_m fL(\omega)}{1 - c_p fL(\omega)}, \quad (6)$$

where c_m and c_p are $c_m = (\epsilon_b - \epsilon_m)^{-1}$ and $c_p = (\epsilon_b + 2\epsilon_m)^{-1}$, respectively. It is possible to write $\chi(\omega)$ in the form

$$\chi(\omega) = 1 + fA \frac{L(\omega)}{1 - c_p fL(\omega)}, \quad (7)$$

where $A = -3\epsilon_m c_p c_m$. Using this result, we can decompose the right-hand side of Eq. (5) into two parts as

$$\frac{\epsilon(\omega) - \epsilon_m}{\epsilon(\omega) + 2\epsilon_m} = \frac{\epsilon_b - \epsilon_m}{\epsilon_b + 2\epsilon_m} - \frac{3\epsilon_m fL(\omega)}{(\epsilon_b + 2\epsilon_m)[(\epsilon_b + 2\epsilon_m) - fL(\omega)]}. \quad (8)$$

For given values of ϵ_b and ϵ_m , the first term gives a constant representing a nonresonant component of the scattered wave, which persists even when $f = 0$ (no excitonic transition), while the second term describes an ω -dependent resonant component arising from the exciton excitation, which vanishes when $f = 0$. Since Q_{sca} given by Eq. (2) is proportional to the square of the absolute value of Eq. (8), we can expect that Q_{sca} exhibits a Fano line shape caused by the interference between the nonresonant and resonant components of the scattered wave. The line shape is determined by the relative magnitudes of the nonresonant and resonant components and their phase difference.

To derive the Fano line shape function for Q_{sca} , it is convenient to introduce a background scattering efficiency corresponding to the case of $f = 0$ defined by

$$Q_{\text{back}} = \frac{8}{3}x^4 \left(\frac{\epsilon_b - \epsilon_m}{\epsilon_b + 2\epsilon_m} \right)^2. \quad (9)$$

Note that Q_{back} is proportional to x^4 and thus to $1/\lambda^4$. Q_{back} is nothing but the efficiency of the Rayleigh scattering of a sufficiently small sphere having the background dielectric constant ϵ_b . Writing as $F_{\text{sca}} = |\chi(\omega)|^2$ we can express Q_{sca} as

$$Q_{\text{sca}} = Q_{\text{back}} F_{\text{sca}}. \quad (10)$$

For a sufficiently small value of γ_{exc} , $L(\omega)$ makes a significant contribution to $\epsilon(\omega)$ only in a narrow region around $\omega = \omega_{\text{exc}}$. Therefore, we can approximate the term $i\omega\gamma_{\text{exc}}$ in $L(\omega)$ by $i\omega_{\text{exc}}\gamma_{\text{exc}}$. Under this approximation, $\chi(\omega)$ takes the following form:

$$\chi(\omega) \approx \frac{\omega^2 - \omega_z^2}{\omega^2 - \omega_p^2}, \quad (11)$$

with $\omega_z^2 = \omega_{\text{exc}}^2(1 + c_m f) - i\omega_{\text{exc}}\gamma_{\text{exc}}$ and $\omega_p^2 = \omega_{\text{exc}}^2(1 + c_p f) - i\omega_{\text{exc}}\gamma_{\text{exc}}$, respectively. Note that this form of $\chi(\omega)$ is very similar to that of the optical response functions discussed by Avrutsky *et al.* [30] and Nesterenko *et al.* [31]. When $\omega_F^2 = \omega_{\text{exc}}^2(1 + c_p f)$ and $X = (\omega^2 - \omega_F^2)/\omega_{\text{exc}}\gamma_{\text{exc}}$ are introduced, it is straightforward to derive the following line shape function:

$$F_{\text{sca}}^{\text{ap}} = |\chi(\omega)|^2 = \frac{(X + q)^2 + 1}{X^2 + 1}, \quad (12)$$

with

$$q = \frac{(\omega_p^2 - \omega_z^2)}{\omega_{\text{exc}}\gamma_{\text{exc}}} = fA \frac{\omega_{\text{exc}}}{\gamma_{\text{exc}}} = \frac{-3\epsilon_m f}{(\epsilon_b + 2\epsilon_m)(\epsilon_b - \epsilon_m)} \frac{\omega_{\text{exc}}}{\gamma_{\text{exc}}}. \quad (13)$$

It should be noted that this expression of $F_{\text{sca}}^{\text{ap}}$ is a special case of the generalized Fano function derived from an *ab initio* electromagnetic theory by Gallinet and Martin [32,33], which is written as

$$\sigma_{\text{F}} = \frac{(\Omega + q)^2 + b}{\Omega^2 + 1}, \quad (14)$$

where $\Omega = (\omega^2 - \omega_{\text{F}}^2)/\omega_{\text{F}}\Gamma$ with the position ω_{F} and the width Γ of the Fano resonance, q is the asymmetry parameter, and b is the screening parameter arising from the loss. In fact, σ_{F} reduces to $F_{\text{sca}}^{\text{ap}}$ when b is set to 1 and $\omega_{\text{F}}\Gamma$ in the denominator of Ω is replaced by $\omega_{\text{exc}}\gamma_{\text{exc}}$.

It is now clear that the scattering spectrum of the excitonic sphere is generated by the interference of two components, the nonresonant component corresponding to the Rayleigh scattering of the sphere having the background dielectric constant and the resonant component arising from the exciton excitation. As in Eq. (10), Q_{sca} is given by a product of Q_{back} describing the background Rayleigh scattering and $F_{\text{sca}}^{\text{ap}}$ [Eq. (12)] describing the asymmetric Fano line shape. Within the ES approximation considered here, Q_{back} increases with the radius being proportional to R^4 [Eq. (9)], while $F_{\text{sca}}^{\text{ap}}$ is independent of the radius. The analytical expression of q [Eq. (13)] allows us to easily predict changes in the Fano line shape brought by changes in the parameters ε_{b} , f , ω_{exc} , and γ_{exc} in the excitonic dielectric function, as well as ε_{m} of the surrounding medium.

From the approximate expression of $\chi(\omega)$ given by Eq. (11) we can obtain

$$\text{Im}\chi(\omega) \approx \frac{-Af}{X^2 + 1} \frac{\omega_{\text{exc}}}{\gamma_{\text{exc}}}. \quad (15)$$

When Q_{abs} is factorized by Q_{back} as

$$Q_{\text{abs}} = Q_{\text{back}}F_{\text{abs}}, \quad (16)$$

an approximate form of F_{abs} is simply given by

$$F_{\text{abs}}^{\text{ap}} = \frac{a}{X^2 + 1}, \quad (17)$$

with

$$a = \frac{9\varepsilon_{\text{m}}f}{2x_0^3(\varepsilon_{\text{b}} - \varepsilon_{\text{m}})^2} \frac{\omega_{\text{exc}}}{\gamma_{\text{exc}}}, \quad (18)$$

where x_0 is given by $x_0 = (\omega_{\text{exc}}/c)\sqrt{\varepsilon_{\text{m}}}R$ with the speed of light c . In deriving Eq. (18) λ entering in the expressions of Q_{abs} [Eq. (3)] and Q_{back} [Eq. (9)] though the size parameter x was replaced by λ_{exc} and converted to ω_{exc} , since $\text{Im}\chi(\omega)$ makes significant contributions only in the vicinity of $\omega = \omega_{\text{exc}}$. The above equations indicate that the absorption spectrum Q_{abs} exhibits a Lorentzian line shape $F_{\text{abs}}^{\text{ap}}$ superposed on the Rayleigh background Q_{back} .

Using the above results, it is easy to obtain the line shape function for $Q_{\text{ext}} = Q_{\text{sca}} + Q_{\text{abs}}$. In the same way as Q_{sca} and Q_{abs} , we factorize as

$$Q_{\text{ext}} = Q_{\text{back}}F_{\text{ext}}. \quad (19)$$

Then, the line shape function $F_{\text{ext}}^{\text{ap}}$ is given by

$$F_{\text{ext}}^{\text{ap}} = F_{\text{sca}}^{\text{ap}} + F_{\text{abs}}^{\text{ap}} = \frac{(X + q)^2 + (1 + a)}{X^2 + 1}. \quad (20)$$

This functional form is identical to the generalized Fano function given by Eq. (14) when $1 + a$ is rewritten as b and $\omega_{\text{exc}}\gamma_{\text{exc}}$ in the denominator of X is replaced by $\omega_{\text{F}}\Gamma$. Since q and b can be calculated analytically using the expressions given above, it is easy to predict changes in the Fano line shape of $F_{\text{ext}}^{\text{ap}}$ caused by changes in the system parameters.

2. General functions describing ε_{m} -dependence of parameters q and a

The Fano line shape described by $F_{\text{sca}}^{\text{ap}}$ [Eqs. (12) and (13)] does not depend on R since q [Eqs. (13)] is independent of R . However, Eq. (13) predicts a strong dependence of q on ε_{m} . To discuss the ε_{m} -dependence of the Fano line shape, it is convenient to introduce a ratio $t = \varepsilon_{\text{m}}/\varepsilon_{\text{b}}$. Then, q is transformed into

$$q = C_q f_q(t), \quad (21)$$

with

$$C_q = \frac{3f}{\varepsilon_{\text{b}}} \frac{\omega_{\text{exc}}}{\gamma_{\text{exc}}}, \quad (22)$$

and

$$f_q(t) = \frac{-t}{(1 + 2t)(1 - t)}. \quad (23)$$

For a given set of the parameters, C_q is a constant. Therefore, the ε_{m} -dependence of q can generally be described by the function $f_q(t)$. The factor $(1 - t)$ contained in the denominator of $f_q(t)$ allows us to predict two important behaviors of q . One is the change in the sign of q ; q is negative for $t < 1$ ($\varepsilon_{\text{m}} < \varepsilon_{\text{b}}$), while it is positive for $t > 1$ ($\varepsilon_{\text{m}} > \varepsilon_{\text{b}}$). Another important behavior is the divergence of q when t (ε_{m}) approaches 1 (ε_{b}). As mentioned before, the Fano line shape arises from the interference between the nonresonant background component [first term of Eq. (8)] and the resonant excitonic component [second term of Eq. (8)] of the scattered wave. The asymmetry parameter q is determined by the relative magnitude and the phase difference of the two components. Equation (8) indicates that the background component is proportional to $\varepsilon_{\text{b}} - \varepsilon_{\text{m}}$ and changes its phase by π depending on the relative magnitudes of ε_{m} and ε_{b} . On the other hand, the excitonic component does not contain the factor $\varepsilon_{\text{b}} - \varepsilon_{\text{m}}$, and shows no abrupt phase change. Therefore, the change in the sign of q is attributed to the π -change in the phase of the nonresonant component. The origin of the factor $(1 - t)$ contained in the denominator of $f_q(t)$ can be traced back to the factorization of Q_{sca} by Q_{back} . Therefore, the physical origin of the divergence of $|q|$ as t (ε_{m}) approaches 1 (ε_{b}) is the disappearance of the background scattering, leaving only the Lorentzian excitonic component; note that the line shape described by the generalized Fano function approaches the Lorentzian line shape as $|q| \rightarrow \infty$.

The parameter a of the Lorentzian function $F_{\text{abs}}^{\text{ap}}$ [Eq. (18)] can also be expressed in terms of t as

$$a = C_a f_a(t), \quad (24)$$

with

$$C_a = \frac{9f}{2y_0^3(\sqrt{\varepsilon_{\text{b}}})^5} \frac{\omega_{\text{exc}}}{\gamma_{\text{exc}}}, \quad (25)$$

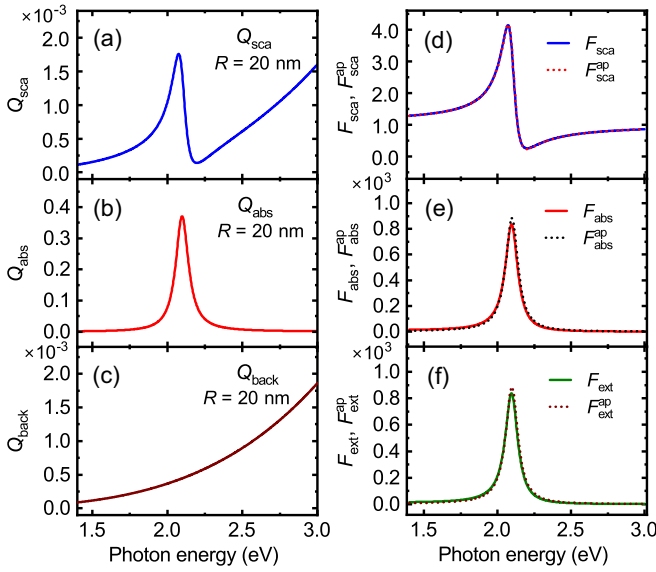


FIG. 2. Spectra of a model excitonic sphere of $R = 20$ nm ($x_{\text{es}} = 0.2$) placed in air ($\epsilon_m = 1$), which mimics a polymer sphere doped with J-aggregates of excitonic molecules, calculated by using Eqs. (2), (3), and (9) of the ES approximation. (a)–(c) display the spectra of Q_{sca} , Q_{abs} , and Q_{back} , respectively. Comparison of F_{sca} , F_{abs} , and F_{ext} spectra with those obtained from approximate line shape functions $F_{\text{sca}}^{\text{ap}}$, $F_{\text{abs}}^{\text{ap}}$, and $F_{\text{ext}}^{\text{ap}}$; comparisons between (d) F_{sca} and $F_{\text{sca}}^{\text{ap}}$, (e) F_{abs} and $F_{\text{abs}}^{\text{ap}}$, and (f) F_{ext} and $F_{\text{ext}}^{\text{ap}}$, respectively.

and

$$f_a(t) = \frac{1}{\sqrt{t}(1-t)^2}, \quad (26)$$

where y_0 is given by $y_0 = (\omega_{\text{exc}}/c)R$. Since C_a is a constant for a given set of the parameters, the function $f_a(t)$ describes generally the ϵ_m -dependence of a . Because of the factor $(1-t)^{-2}$ in $f_a(t)$, a is predicted to diverge at $t = 1$. The origin of this factor can also be traced back to the factorization of Q_{abs} by Q_{back} . We can thus attribute the divergence of a at $t = 1$ to the disappearance of the background scattering. Note that the factorization by Q_{back} also introduces a R^{-3} -dependence into a .

3. Spectra of a model excitonic sphere

To perform realistic numerical calculations of spectra we consider a model excitonic sphere that mimics a polymer sphere doped with J-aggregates of dye molecules. We assume the following parameters of the excitonic dielectric function $\epsilon(\omega)$: $\hbar\omega_{\text{exc}} = 2.0664$ eV (corresponding to an exciton wavelength of $\lambda_{\text{exc}} = 600$ nm), $\hbar\gamma_{\text{exc}} = 103.32$ meV (corresponding to $\gamma_{\text{exc}}/\omega_{\text{exc}} = 0.05$), $f = 0.13$, and $\epsilon_b = 2.2$. These values were chosen because they are very close to those of poly(vinyl alcohol) thin films doped with J-aggregates of 5, 5', 6, 6'-tetrachloro-1, 1'-diethyl-3, 3'-di(4-sulfobutyl)-benzimidazolocarboyanine (TDBC) molecules [27], a typical example of excitonic materials. Figures 2(a), 2(b), and 2(c) show spectra of Q_{sca} , Q_{abs} , and Q_{back} calculated by using Eqs. (2), (3), and (9), respectively. In the calculations, an excitonic sphere of radius $R = 20$ nm placed in air ($\epsilon_m = 1$) was assumed. To estimate the size parameter of the sphere in a simple manner, it is convenient to

choose a sampling wavelength of the incident light at $\lambda_{\text{es}} = 2\pi \times 100$ nm (≈ 628.3 nm, corresponding to a photon energy of ≈ 1.973 eV), which is close to the exciton wavelength (600 nm). The size parameter estimated at λ_{es} is simply given by $x_{\text{es}} = \sqrt{\epsilon_m}R'/100$, where R' denotes the value of R without the nm unit. Therefore, for $R = 20$ nm and $\epsilon_m = 1$ we obtain $x_{\text{es}} = 0.2$. It should be noted that, for the range of photon energy shown in Fig. 2 and in similar figures shown later, x falls in the range $0.7096x_{\text{es}} \leq x \leq 1.520x_{\text{es}}$. The spectrum of Q_{abs} [Fig. 2(b)] exhibits a Lorentzian line corresponding to the exciton excitation, while that of Q_{back} [Fig. 2(c)] shows a monotonous increase toward the larger photon energies obeying the $(\hbar\omega)^4$ -law of Rayleigh scattering. The spectrum of Q_{sca} [Fig. 2(a)] no longer exhibits the Lorentzian line shape, but clearly exhibits an asymmetric line shape superposed on the Rayleigh background.

In Figs. 2(d), 2(e), and 2(f), the spectra of F_{sca} , F_{abs} , and F_{ext} obtained by normalizing Q_{sca} , Q_{abs} , and Q_{ext} to Q_{back} are compared with those calculated by using the line shape functions $F_{\text{sca}}^{\text{ap}}$, $F_{\text{abs}}^{\text{ap}}$, and $F_{\text{ext}}^{\text{ap}}$ given by Eqs. (12), (17), and (20), respectively. Figure 2(d) demonstrates that F_{sca} can be well reproduced by the Fano function $F_{\text{sca}}^{\text{ap}}$. The Fano line shape was generated by a value of $q = -1.5476$ obtained from Eq. (13) with the assumed values of the parameters. We define the maximum deviation of $F_{\text{sca}}^{\text{ap}}$ from F_{sca} by $\Delta_{\text{sca}}^{\text{max}} = \max|F_{\text{sca}}^{\text{ap}} - F_{\text{sca}}|/\max F_{\text{sca}}$. According to our detailed analyses, the maximum deviation takes place at the steep part of the spectra, due to a small shift of $F_{\text{sca}}^{\text{ap}}$ relative to F_{sca} ; $\Delta_{\text{sca}}^{\text{max}}$ was found to be 1.74%. This deviation is small enough (too small to be seen in the figure) to conclude that the line shape function $F_{\text{sca}}^{\text{ap}}$ is capable of representing the overall line shape of F_{sca} obtained in the ES approximation.

As can be seen in Figs. 2(e), the spectrum of F_{abs} can be well reproduced by the Lorentzian function $F_{\text{abs}}^{\text{ap}}$, which was generated by a value of $a = 884.40$ obtained from Eq. (18) with the parameter values. The maximum deviation, defined in the same way as for $F_{\text{sca}}^{\text{ap}}$, is found at the steep part of the larger energy side of the Lorentzian line shape (not around the maximum of the Lorentzian line shape); $\Delta_{\text{abs}}^{\text{max}}$ is estimated to be 8.10%. The spectrum of F_{ext} ($=F_{\text{sca}} + F_{\text{abs}}$) shown in Fig. 2(f) is essentially the same as that of F_{abs} shown in Fig. 2(e), since the contribution of F_{sca} is about 200 times smaller than that of F_{abs} . The line shape of F_{ext} is very close to the Lorentzian shape, but can be well reproduced by the generalized Fano function $F_{\text{ext}}^{\text{ap}}$ [Eq. (20)] with $q = -1.5476$, which is identical to that of $F_{\text{sca}}^{\text{ap}}$, and $a + 1 = 885.40$. The estimated $\Delta_{\text{ext}}^{\text{max}}$ value is 8.09%. Although the maximum deviations for $F_{\text{abs}}^{\text{ap}}$ and $F_{\text{ext}}^{\text{ap}}$ are larger than that for $F_{\text{sca}}^{\text{ap}}$, Figs. 2(e) and 2(f) demonstrate that the line shape functions $F_{\text{abs}}^{\text{ap}}$ and $F_{\text{ext}}^{\text{ap}}$ are capable of well describing the spectra of F_{abs} and F_{ext} obtained in the ES approximation. The results presented in Figs. 2(d), 2(e), and 2(f) validate the use of the line shape functions in describing the spectra of the small particle limit in simple manners using the parameters q and a .

B. Beyond the small-particle limit

1. Size dependence of spectra

Based on the exact Mie theory, we extended our spectral calculations to the size range beyond the small particle

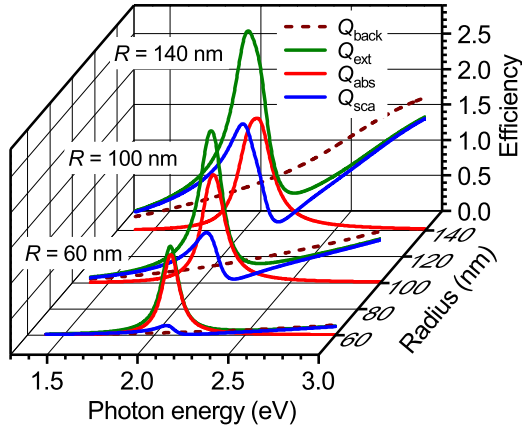


FIG. 3. Spectra of Q_{sca} , Q_{abs} , Q_{ext} , and Q_{back} calculated by the exact Mie theory for the model sphere of $R = 60, 100,$ and 140 nm ($x_{es} = 0.6, 1.0,$ and 1.4) placed in air.

limit. We find that for $R < 50$ nm ($x_{es} < 0.5$), the spectra of Q_{sca} , Q_{abs} , Q_{ext} , and Q_{back} (Q_{sca} obtained with $f = 0$) for the present model excitonic sphere are practically the same as those of the small particle limit. However, around $R = 50$ nm ($x_{es} = 0.5$) the spectra start to deviate from those of the small-particle limit and the deviation becomes more and more pronounced as R increases. Therefore, the ES approximation is no longer valid for the present excitonic sphere for $R > 50$ nm ($x_{es} > 0.5$). The deviation is caused by increasing contributions of higher-order electric modes and magnetic modes of the sphere, in addition to the lowest electric dipole mode that determines the spectra of the ES approximation. Figure 3 shows the spectra of Q_{sca} , Q_{abs} , Q_{ext} , and Q_{back} obtained from the exact Mie theory for $R = 60, 100,$ and 140 nm (corresponding to $x_{es} = 0.6, 1.0,$ and 1.4 , respectively). We see that the spectrum of Q_{abs} exhibits a Lorentzian line and its maximum value increases gradually as R increases. On the other hand, the spectrum of Q_{sca} exhibits an asymmetric line; as R increases, the maximum value increases rapidly along with the overall increase of Q_{back} . The line shape of Q_{ext} ($= Q_{sca} + Q_{abs}$) tends to change from the Lorentzian to asymmetric one since the contribution of Q_{sca} relative to that of Q_{abs} increases rapidly with the increase of R ; the maximum value of Q_{ext} increases rapidly caused by the rapid increase in the Q_{sca} . For the value of $\epsilon_b = 2.2$ assumed for the present excitonic sphere, the spectra of Q_{back} for $R < 150$ nm ($x_{es} < 1.5$) do not exhibit distinct resonant peaks and increase monotonously towards higher energies. However, our detailed analyses of the spectra show that they no longer obey exactly the $(\hbar\omega)^4$ -law of Rayleigh scattering and the deviation from the Rayleigh scattering is more and more pronounced as R increases.

To perform detailed analyses of the line shapes we adopt here the same factorizations of Q_{sca} , Q_{abs} , and Q_{ext} as those introduced in analyzing the spectra of the small-particle limit [Eqs. (10), (16), and (19)]. In Figs. 4(a) to 4(c), spectra of F_{sca} , F_{abs} , and F_{ext} obtained from the exact Mie theory are shown for various R varying from 60 to 140 nm with a step of 20 nm (x_{es} varying from 0.6 to 1.4 with a step of 0.2). Figure 4(a) demonstrates that, in contrast to the size-independent

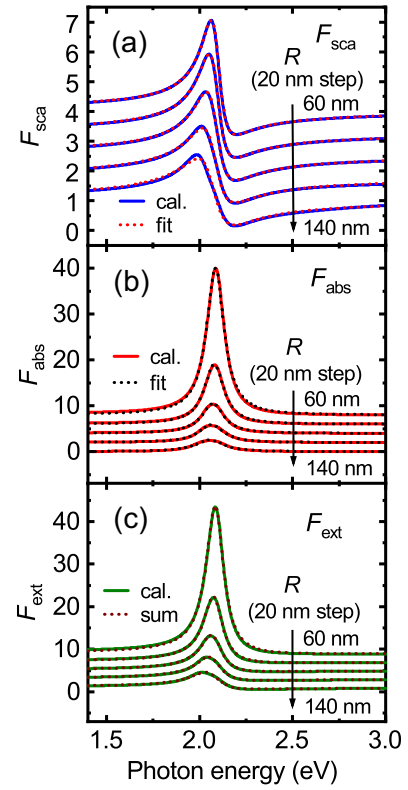


FIG. 4. Spectra of (a) F_{sca} , (b) F_{abs} , and (c) F_{ext} obtained from the exact Mie theory for the sphere of various R varying from 60 to 140 nm with a step of 20 nm (x_{es} varying from 0.6 to 1.4 with a step of 0.2). The spectra are displayed with vertical offsets; the offset value is 1.0 for (a) and 2.0 for (b) and (c). In (a), the spectra of F_{sca} are compared with curves resulting from fitting to the generalized Fano function, while in (b) the spectra of F_{abs} are compared with those resulting from fitting to the Lorentzian function. In (c), the spectra of F_{ext} are compared with curves obtained by summing the fit results of F_{sca} and F_{abs} .

spectrum of the small-particle limit [Fig. 2(d)], the spectrum of F_{sca} significantly changes depending on R . In fact, the spectrum for $R = 60$ nm ($x_{es} = 0.6$) is still very close to that of the small-particle limit [Fig. 2(d)], but as R increases, the height of resonance (the difference between the maximum and the minimum) decreases and the steep part of the spectrum at the high-energy side becomes less steep. These changes in the spectral shape suggest the change in the asymmetry parameter q , when the Fano function is applied to describe the asymmetric line shape.

In Sec. A.1, we show that the approximate line shape functions F_{sca}^{ap} and F_{ext}^{ap} for F_{sca} and F_{ext} in the ES approximation take the forms of the generalized Fano function, while F_{abs}^{ap} for F_{abs} is expressed by the Lorentzian function. It should be remembered that the asymmetry parameter q in F_{sca}^{ap} and F_{ext}^{ap} takes the restricted values determined by Eq. (13). The amplitude a of the Lorentzian function for F_{abs}^{ap} also takes the restricted values determined by Eq. (18). Furthermore, the asymmetry parameter b in F_{sca}^{ap} is fixed at $b = 1.0$ [Eq. (12)] and that in F_{ext}^{ap} at $b = a + 1$ [Eq. (20)]. Beyond the small-particle limit, these approximate line shape functions are expected to be no longer valid. However, it seems that

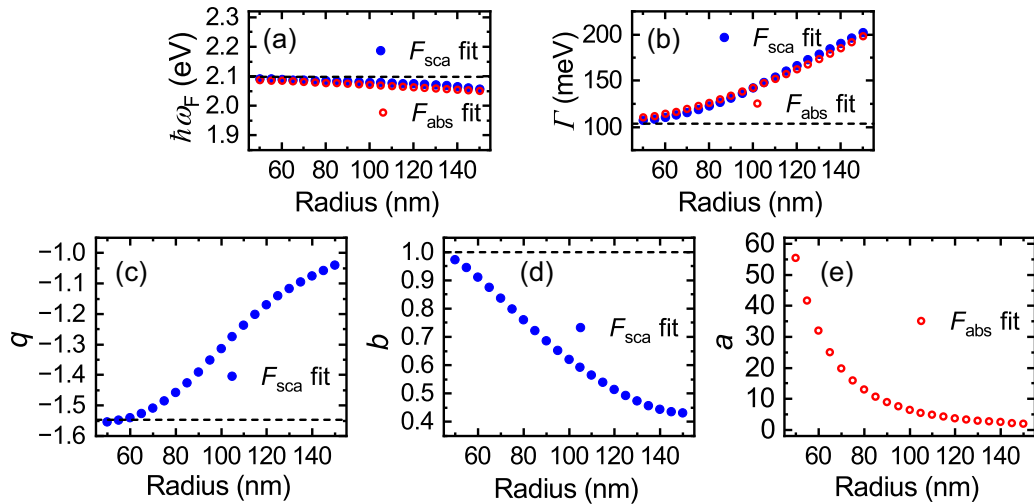


FIG. 5. R -dependencies of the fitting parameters. (a) ω_F and (b) Γ for both the generalized Fano function and Lorentzian function, (c) q and (d) b for the generalized Fano function and (e) a for the Lorentzian function. Values of the parameters in the small-particle limit are presented by horizontal broken lines. These figures cover the range $0.5 \leq x_{es} \leq 1.5$.

the spectra of F_{sca} beyond the small-particle limit shown in Fig. 4(a) preserve the Fano line shape. Therefore, we attempt to fit the spectra to the generalized Fano function given by Eq. (14) by setting the parameters ω_F , Γ , q , and b as free parameters, instead of restricting their values to those of the small-particle limit.

We perform least-square fitting of F_{sca} spectra obtained by varying R with a step of 5 nm in the range $50 \text{ nm} \leq R \leq 150 \text{ nm}$ ($0.5 \leq x_{es} \leq 1.5$ with a step of 0.05). In Fig. 4(a), the resulting fit curves are compared with the F_{sca} spectra. Fit parameters obtained are plotted as a function of R in Figs. 5(a) to 5(d). In these figures, the horizontal broken lines indicate the parameters that reproduce the spectrum of the small particle limit. A close look at Fig. 4(a) reveals that the F_{sca} spectra except for that of $R = 140 \text{ nm}$ ($x_{es} = 1.4$) can be well reproduced by the generalized Fano function. However, for $R = 140 \text{ nm}$, deviation of F_{sca} spectrum from the fit curve becomes discernible, in particular, near the maximum, implying that the F_{sca} spectrum starts to deviate from the Fano line shape at about $R = 140 \text{ nm}$ ($x_{es} = 1.4$). We find that, as R increases further, the deviation is more and more pronounced and the deformation of the line shape from the Fano line shape becomes apparent.

Figures 5(a) to 5(d) demonstrate that all the parameters in the generalized Fano function, ω_F , Γ , q , and b , start to deviate from the ES values at about $R = 50 \text{ nm}$ ($x_{es} = 0.5$) and the deviation becomes larger as R increases. As mentioned earlier, in the small-particle limit, the optical responses are determined by the lowest-order Mie coefficient a_1 . However, for the sphere with $R > 50 \text{ nm}$ ($x_{es} > 0.5$), b_1 and higher-order a_n and b_n Mie coefficients come to contribute and their contributions become more and more important as R increases, leading to the deviations of the F_{sca} spectra and the fitting parameters from those of the small particle limit. Nevertheless, the results presented in Fig. 4(a) and Figs. 5(a) to 5(d) demonstrate that the generalized Fano function is capable of describing well the asymmetric line shape of the F_{sca} spectrum as long as R is smaller than a certain upper bound value. It is difficult to determine precisely the upper bound value. However, the

upper bound for the present excitonic sphere can be set at about $R_{\text{bound}} = 130 \text{ nm}$ ($x_{es} = 1.3$).

Since the spectra of F_{abs} shown in Fig. 4(b) appear to be Lorentzian, we use the following Lorentzian function to fit the spectra:

$$\sigma_L = \frac{a}{\Omega^2 + 1}, \quad (27)$$

where $\Omega = (\omega^2 - \omega_F^2)/\omega_F\Gamma$ and a is taken as a free parameter. The fit curves are compared with the F_{abs} spectra in Fig. 4(b). The fit parameters, ω_F , Γ , and a obtained for the F_{abs} spectra with R ranging in $50 \text{ nm} \leq R \leq 150 \text{ nm}$ ($0.5 \leq x_{es} \leq 1.5$) are plotted in Figs. 5(a), 5(b), and 5(e), respectively. Figure 4(b) demonstrates that the Lorentzian fit curves reproduce very well all the F_{abs} spectra presented in the figure. In Fig. 4(c), the spectra of F_{ext} are compared with the curves obtained by summing the Fano fit curves of F_{sca} and the Lorentzian fit curves of F_{abs} . We see that the summed curves reproduce well the F_{ext} spectra. As can be seen in Figs. 5(a) and 5(b), the parameters ω_F and Γ obtained from the fitting are almost identical for the F_{sca} and F_{abs} spectra. This fact allows us to use a generalized Fano function as the line shape function of F_{ext} since a summation of the generalized Fano function representing F_{sca} and the Lorentzian function representing F_{abs} is mathematically proven to be a generalized Fano function; the asymmetric parameter q of the generated function is the same as that for F_{sca} , and the screening parameter is given by $b' = b + a$, where b is the screening parameter for F_{sca} and a is the amplitude parameter for F_{abs} . We note here that the generation of a Fano line shape in extinction spectra by a summation of a Fano line shape of scattering and a Lorentzian line shape of absorption was already reported by Ruan and Fan [34] who compared the spectra for a metal-dielectric-metal cylinder obtained from the exact Mie theory and a temporal coupled-mode theory; Arruda *et al.* [35] calculated the spectra of a silver nanoshell based on the exact Mie theory and reported a Fano line shape generated by the same mechanism.

From the results presented above, we can conclude that even beyond the small-particle limit, the scattering and

extinction spectra of the excitonic sphere can be well described by the generalized Fano function, while the absorption spectra can be well described by the Lorentzian function. This conclusion is valid for R smaller than the upper bound R_{bound} . According to our detailed analyses, the R_{bound} becomes smaller as ε_b increases. We note that, for a value of ε_b as large as 16, which is the case of high-index materials like Si and GaP crystals, the R_{bound} is as small as 30 nm ($x_{\text{es}} = 0.3$). For R entering in the range of $60 \text{ nm} \leq R \leq 130 \text{ nm}$ ($0.6 \leq x_{\text{es}} \leq 1.3$), for example, the spectra of Q_{back} of high-index spheres exhibit pronounced peaks attributed to the excitation of the electric dipole, magnetic dipole, and higher-order modes in the visible region, and they shift to lower energies as R increases [14,36–38]. Our calculations show that the magnetic dipole (electric dipole) resonance overlaps the exciton resonance at 2.0664 eV ($\lambda = 600 \text{ nm}$) around $R = 70 \text{ nm}$ ($x_{\text{es}} = 0.7$) [95 nm ($x_{\text{es}} = 0.95$)]. Under these conditions, scattering, absorption and extinction spectra exhibit features much different from those presented above. Around the exciton energy, instead of the asymmetric line shapes, dips are observed in the scattering and extinction spectra, while the absorption peak is split into two. These spectral features can neither be described by the Lorentzian function nor by the Fano function. The splitting of the absorption peaks suggest relatively strong coupling between the electromagnetic modes of the sphere with the excitonic transition, which deserves further detailed studies.

2. Dependence of spectra on the dielectric constant of surrounding medium

Assuming the model excitonic sphere of $R = 100 \text{ nm}$, we studied systematically the dependence of the spectra on the dielectric constant of the surrounding medium ε_m . Spectra of Q_{sca} , Q_{abs} , Q_{ext} , and Q_{back} obtained for $\varepsilon_m < \varepsilon_b$ ($\varepsilon_b = 2.2$) and $\varepsilon_m > \varepsilon_b$ are shown in Figs. 6(a) and 6(b), respectively. Note that for $R = 100 \text{ nm}$, the size parameter is estimated at the sampling wavelength is simply given by $x_{\text{es}} = \sqrt{\varepsilon_m}$; therefore, the results shown in Figs. 6(a) and 6(b) cover the range of x_{es} from 1.0 to 2.0. These figures demonstrate drastic changes in the spectra depending on ε_m . We note that the spectrum of Q_{back} approaches zero as ε_m approaches ε_b from larger and smaller values. This behavior of Q_{back} is natural because, when a sphere having ε_b is embedded in a medium of ε_b , optically there is no boundary and thus no scattering. Along with the change in Q_{back} , Q_{sca} changes dramatically; the most drastic change in the line shape is the reversal of the peak and valley positions in the asymmetric line shape, as can be clearly seen from a comparison of the Q_{sca} spectra corresponding to $\varepsilon_m = 1.0$ and 4.0. All the Q_{sca} spectra shown in Figs. 6(a) and 6(b) are asymmetric, but tend to be less asymmetric and approach the Lorentzian line shape as ε_m approaches ε_b . The spectra of Q_{abs} exhibit symmetric lines and the maximum value increases monotonously as ε_m increases. The spectra of Q_{ext} given by $Q_{\text{sca}} + Q_{\text{abs}}$ are asymmetric and inherit the ε_m -dependence of Q_{sca} , but they are less asymmetric because of the contribution of the symmetric spectra of Q_{abs} .

The spectra of F_{sca} , F_{abs} , and F_{ext} obtained for various values of ε_m smaller than ε_b are shown in Figs. 7(a), 7(b), and 7(c), respectively, while the spectra obtained for various

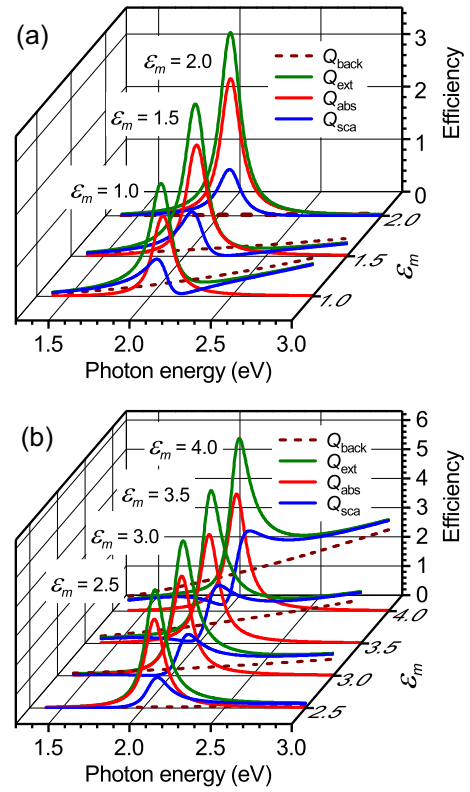


FIG. 6. ε_m -dependencies of Q_{sca} , Q_{abs} , Q_{ext} , and Q_{back} spectra calculated by the exact Mie theory for the model sphere of $R = 100 \text{ nm}$. Spectra corresponding to (a) $\varepsilon_m < \varepsilon_b$ and (b) $\varepsilon_m > \varepsilon_b$ for ε_m values indicated in the figures. For $R = 100 \text{ nm}$, values of x_{es} are simply given by $\sqrt{\varepsilon_m}$.

values of ε_m larger than ε_b are shown in Figs. 7(d), 7(e), and 7(f). Comparisons between Figs. 7(a) and 7(d), and between Figs. 7(c) and 7(f), clearly reveal the reversal of the peak and valley positions in the F_{sca} and F_{ext} spectra, respectively. For all of the spectra shown in Fig. 7, we see the increase of the peak values as ε_m approaches ε_b ; this is due to the factorization of Q_{sca} , Q_{abs} , and Q_{ext} by decreasing Q_{back} in obtaining F_{sca} , F_{abs} , and F_{ext} .

The spectra of F_{sca} and F_{abs} were calculated by varying ε_m with a step of 0.1 in the range $1.0 \leq \varepsilon_m \leq 4.0$ ($1.0 \leq x_{\text{es}} \leq 2.0$). The resulting spectra were fitted to the generalized Fano function and the Lorentzian function, respectively. The resulting fitting parameters are plotted in Figs. 8(a) to 8(e). Comparisons between the fit curves and the spectra of F_{sca} [Figs. 7(a) and 7(d)] and those of F_{abs} [Figs. 7(b) and 7(e)] reveal that the fit curves reproduce very well the spectra. As shown in Figs. 7(c) and 7(f), the spectra of F_{ext} are very well reproduced by curves obtained by summing the fit curves of F_{sca} and F_{abs} . The results presented in Fig. 7 again confirm the suitability of the generalized Fano function and the Lorentzian function to describe the spectra of F_{sca} and F_{abs} , respectively, even beyond the small particle limit provided that $R < R_{\text{bound}}$.

In Figs. 8(c) and 8(e), ε_m -dependencies of q and a determined by the fitting are plotted together with those calculated by the analytical expressions of the ES approximation [Eqs. (13) or (21) for q and Eqs. (18) or (24) for a]. We see that the results of fitting agree qualitatively with those of the

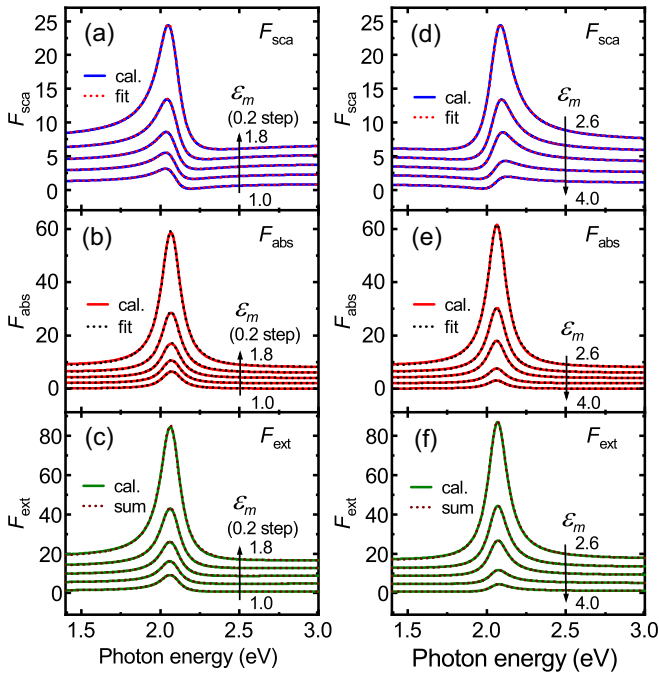


FIG. 7. Spectra of F_{sca} , F_{abs} , and F_{ext} for the model sphere of $R = 100$ nm obtained from the exact Mie theory by varying ϵ_m ($x_{es} = \sqrt{\epsilon_m}$). (a)–(c) are for ϵ_m values varying from 1.0 to 1.8 with a step of 0.2 ($\epsilon_m < \epsilon_b$). The spectra are displayed with vertical offsets; the offset value is 2.0 for (a) and (b), and 4.0 for (c), respectively. (d)–(f) are for $\epsilon_m = 2.6, 2.8, 3.0, 3.5,$ and 4.0 ($\epsilon_m > \epsilon_b$); the offset value is 2.0 for (d) and (e), and 4.0 for (f), respectively. In (a) and (d), the spectra of F_{sca} are compared with curves resulting from fitting to the generalized Fano function, while in (b) and (e) the spectra of F_{abs} are compared with those resulting from fitting to the Lorentzian function. In (c) and (f), the spectra of F_{ext} are compared with the curves obtained by summing the fit curves of F_{sca} and F_{abs} .

ES approximation. As already pointed out in Sec. II A 2, the divergence of q and a at $\epsilon_m = \epsilon_b$ is due to the disappearance of the background scattering. The change in the sign of q is attributed to the π -change in the phase of background scattered wave. Although these points were deduced within the ES approximation, the qualitative agreements of the fitting results with the ES results suggest that the disappearance of the background scattering at $\epsilon_m = \epsilon_b$, which is also true beyond the small-particle limit, is the cause of the divergence of q and a . Furthermore, the π -change in the phase of background scattered wave is anticipated to be the cause of the change in the sign of q . As can be seen in Fig. 8(d), in contrast to the above qualitative agreements of q and a , the ϵ_m dependence of the screening parameter b resulting from the fitting deviates from that of the ES approximation ($b = 1$) around $\epsilon_m = \epsilon_b$. Clear explanation about this deviation is lacking at present and deserve further detailed studies. The fitting results of ω_F plotted in Fig. 8(a) indicate that ω_F is almost identical for F_{sca} and F_{abs} . In Fig. 8(b), we see that the fitting results of Γ for F_{sca} slightly differ from those of F_{abs} ; the maximum difference is estimated to be $\sim 13.1\%$. This small difference allows us to use the generalized Fano function constructed by adding that of F_{sca} and the Lorentzian function of F_{abs} to approximately describe the ϵ_m -dependence of F_{ext} . The results

presented above indicate that, even beyond the small-particle limit, the ϵ_m -dependence of F_{abs} can be well described by the Lorentzian function, while that of F_{sca} and F_{ext} can be described by the generalized Fano function, provided that $R < R_{bound}$. We note finally that the strong dependence of Q_{sca} and Q_{ext} spectra on ϵ_m shown here opens up a possibility of developing a single-particle sensor of the refractive index (or dielectric constant) of the surrounding medium by effectively monitoring the changes in the spectra.

III. SPECTRA OF INTERNAL FIELDS

A. Electrostatics approximation

We now proceed to analyze the behaviors of internal fields; the basic equations of the Mie theory necessary for the analysis are summarized in the Supplemental Material [29]. We consider here the local field-enhancement factor defined by

$$FE_{local}(\mathbf{r}) = \frac{|\mathbf{E}_1(\mathbf{r})|^2}{|E_0|^2}, \quad (28)$$

where $\mathbf{E}_1(\mathbf{r})$ is the local electric field induced at a position \mathbf{r} inside the sphere and E_0 is the electric field amplitude of the incident light. In the small-particle limit, since $\mathbf{E}_1(\mathbf{r})$ is uniform over the sphere, $FE_{local}(\mathbf{r})$ is also uniform. Omitting the subscript and using the expression of the electric field given by Eq. (S13) of the Supplemental Material [29], we can simply express the uniform field enhancement factor as

$$FE = \left| \frac{3\epsilon_m}{\epsilon(\omega) + 2\epsilon_m} \right|^2. \quad (29)$$

In the same way as Eq. (5), we can write

$$\frac{3\epsilon_m}{\epsilon(\omega) + 2\epsilon_m} = \left(\frac{3\epsilon_m}{\epsilon_b + 2\epsilon_m} \right) \zeta(\omega), \quad (30)$$

with

$$\zeta(\omega) = 1 + fc_p \frac{L(\omega)}{1 - c_p f L(\omega)}. \quad (31)$$

Note that when A in $\chi(\omega)$ [Eq. (7)] is replaced by c_p , $\chi(\omega)$ becomes identical to $\zeta(\omega)$. From Eqs. (30) and (31) it is clear that FE is determined by the interference between the non-resonant background component and the resonant excitonic component. With the aid of FE_{back} defined by

$$FE_{back} = \left(\frac{3\epsilon_m}{\epsilon_b + 2\epsilon_m} \right)^2, \quad (32)$$

FE can be written as

$$FE = FE_{back} F_{int}, \quad (33)$$

with

$$F_{int} = |\zeta(\omega)|^2. \quad (34)$$

An approximate expression of F_{int} , written as F_{int}^{ap} , can easily be obtained, when the term $i\omega\gamma_{exc}$ in $L(\omega)$ is approximated by $i\omega_{exc}\gamma_{exc}$ and the procedures for deriving F_{sca}^{ap} from $\chi(\omega)$ described in Sec. II A 1 are applied to $\zeta(\omega)$. In fact, we find that F_{int}^{ap} takes the form of the generalized Fano function, exactly the same form as for F_{sca}^{ap} [Eq. (12)], but with a different

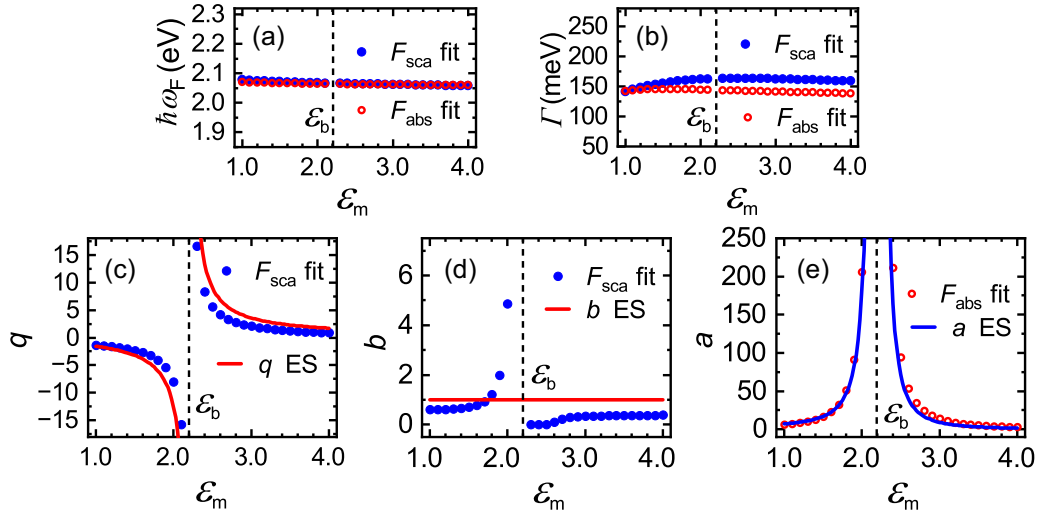


FIG. 8. ε_m -dependencies of the fitting parameters. (a) ω_F and (b) Γ for both the generalized Fano function and Lorentzian function, (c) q and (d) b for the generalized Fano function and (e) a for the Lorentzian function. In (c)–(e), solid lines show behaviors of the parameters predicted in the ES approximation. The range of ε_m shown in the figures corresponds to the range of x_{es} from 1.0 to 2.0.

expression of the asymmetry parameter q ,

$$q = fc_p \frac{\omega_{exc}}{\gamma_{exc}}. \quad (35)$$

It should be noted that in the ES approximation, in contrast to Q_{sca} and Q_{back} , which depend on R through x^4 , the expressions of FE and FE_{back} do not contain x , and consequently, they are independent of R . In a manner similar to Eq. (21), q of F_{int}^{ap} can be written as

$$q = C_q^{int} f_q^{int}(t), \quad (36)$$

with

$$C_q^{int} = \frac{f}{\varepsilon_b} \frac{\omega_{exc}}{\gamma_{exc}}, \quad (37)$$

and

$$f_q^{int}(t) = \frac{1}{1 + 2t}. \quad (38)$$

The above equations predict that, for a given set of parameter values, q takes a positive value and decreases monotonously as $t (= \varepsilon_m/\varepsilon_b)$ increases: this behavior is very much different from that of q for F_{sca}^{ap} , which diverges around $t = 1$ due to the disappearance of the background scattering and changes its sign caused by the π -change in the phase of background scattering.

For the model excitonic sphere placed in air, we calculated the spectra of FE , FE_{back} , F_{int} , and F_{int}^{ap} . Figure 9(a) shows the spectra of FE and FE_{back} , while in Fig. 9(b) the corresponding spectra of F_{int} and F_{int}^{ap} are compared. In contrast to Q_{back} , which obeys the $1/\lambda^4$ -law of the Rayleigh scattering, FE_{back} is flat as seen in Fig. 9(a). Figure 9(b) shows that the spectrum of F_{int} is well reproduced by the Fano function F_{int}^{ap} ; the Fano line shape was generated by a value of $q = 0.61905$ obtained from Eq. (35) with the assumed values of the parameters. Note that the positions of the peak and valley in the spectrum of F_{int} are reversed relative to those of F_{sca} in Fig. 2(d), consistent with a

positive value of q for F_{int}^{ap} and a negative value for F_{sca}^{ap} . The maximum error for F_{int}^{ap} was estimated to be $\Delta_{int}^{max} = 1.98\%$, which is of the same order of magnitude as that for F_{sca}^{ap} .

B. Beyond the small-particle limit

1. Average field-enhancement factor

Beyond the small-particle limit, the local electric field inside a sphere is no longer uniform. In this case, it is convenient to introduce the average field-enhancement factor obtained by averaging the local field-enhancement factor $FE_{local}(\mathbf{r})$ [Eq. (28)] over the sphere volume as

$$FE^{av} = \frac{1}{V} \int_0^R \int_0^\pi \int_0^{2\pi} FE_{local}(\mathbf{r}) r^2 \sin\theta dr d\theta d\phi, \quad (39)$$

where V is the volume of the sphere. Using the expression of $\mathbf{E}_l(\mathbf{r})$ given by Eq. (S11) in the Supplemental Material [29]

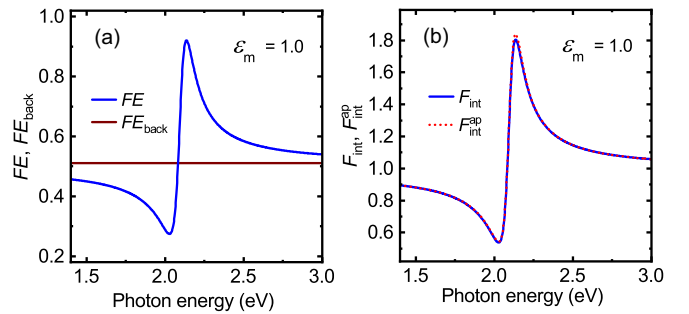


FIG. 9. Spectra of a model excitonic sphere placed in air ($\varepsilon_m = 1$), calculated using the equations of the ES approximation. (a) FE [Eq. (29)] and FE_{back} [Eq. (32)]. (b) Comparison between F_{int} obtained from Eq. (33) and F_{int}^{ap} obtained from the generalized Fano function [Eq. (12)] with a q value calculated by Eq. (35).

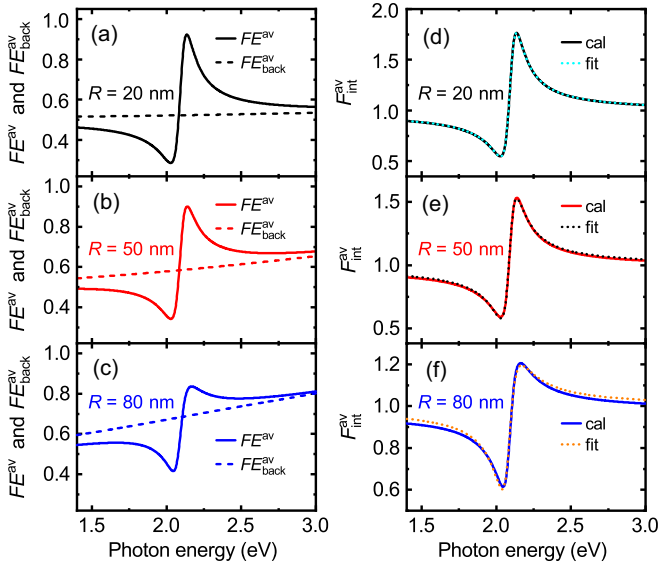


FIG. 10. Spectra of FE^{av} and $FE^{\text{av}}_{\text{back}}$ of the model sphere placed in air for (a) $R = 20$ nm ($x_{\text{es}} = 0.2$), (b) 50 nm ($x_{\text{es}} = 0.5$), and (c) 80 nm ($x_{\text{es}} = 0.8$). In (d)–(f), corresponding spectra of $F_{\text{int}}^{\text{av}}$ are compared with curves resulting from the fitting to the generalized Fano function [Eq. (14)].

and performing the integrations over θ and ϕ [17], we find

$$FE^{\text{av}} = \frac{3}{2} \frac{1}{R^3} \sum_{n=1}^{\infty} \{ |c_n|^2 (2n+1) J_n(R) + |d_n|^2 [n J_{n+1}(R) + (n+1) J_{n-1}(R)] \}, \quad (40)$$

where c_n and d_n are the Mie coefficients describing the local electric fields inside the sphere given by Eqs. (S9) and (S10) in the Supplemental Material [29], respectively, and $J_n(R)$ represents

$$J_n(R) = \int_0^R |j_n(k_1 r)|^2 r^2 dr, \quad (41)$$

with k_1 and $j_n(k_1 r)$ being the wave number in the sphere $2\pi\sqrt{\epsilon(\omega)}/\lambda$ and the spherical Bessel function of order n , respectively. In the same way as Q_{back} beyond the small-particle limit, FE^{av} calculated with $f = 0$ (no excitonic transition) is denoted as $FE^{\text{av}}_{\text{back}}$. In parallel with Q_{sca} , we analyze the spectra by introducing $F_{\text{int}}^{\text{av}}$ obtained from

$$FE^{\text{av}} = FE^{\text{av}}_{\text{back}} F_{\text{int}}^{\text{av}}. \quad (42)$$

2. Numerical results for the model excitonic sphere

For the model sphere, we performed numerical calculations of FE^{av} , $FE^{\text{av}}_{\text{back}}$, and $F_{\text{int}}^{\text{av}}$ spectra using Eqs. (40) and (42). First, we discuss the R -dependence of the spectra for the sphere embedded in air. We found that the spectra remain practically the same when R is increased from 1 to 10 nm. However, for $R > 10$ nm ($x_{\text{es}} > 0.1$) the spectra deviate appreciably from those of smaller spheres, indicating that the ES approximation is no longer valid. The spectra of FE^{av} and $FE^{\text{av}}_{\text{back}}$ calculated for $R = 20, 50,$ and 80 nm ($x_{\text{es}} = 0.2, 0.5,$ and 0.8) are shown in Figs. 10(a), 10(b), and 10(c), respectively, and the corresponding spectra of $F_{\text{int}}^{\text{av}}$ are shown

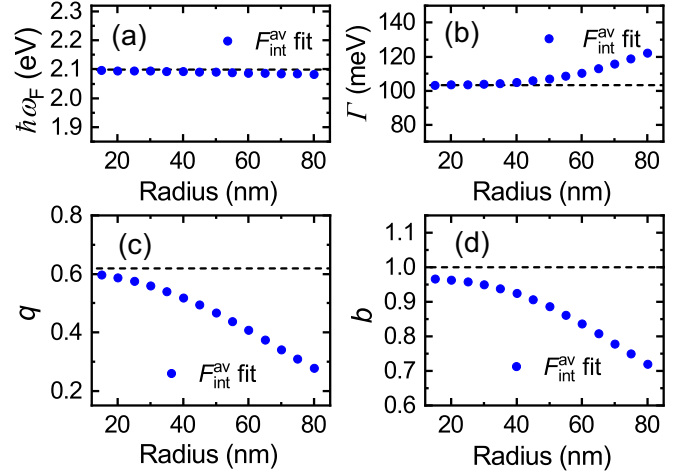


FIG. 11. R -dependencies of the fitting parameters for the generalized Fano function. (a) ω_F , (b) Γ , (c) q , and (d) b . Values of the parameters in the small-particle limit are presented by horizontal broken lines.

in Figs. 10(d), 10(e), and 10(f), respectively. As can be seen from Figs. 10(a), 10(b), and 10(c), the spectrum of $FE^{\text{av}}_{\text{back}}$, which is almost flat for $R = 20$ nm ($x_{\text{es}} = 0.2$), is inclined for larger R and the inclination increases as R increases. Along with the change in the spectrum of $FE^{\text{av}}_{\text{back}}$, the spectrum of FE^{av} changes considerably depending on R . The asymmetric line shapes of $F_{\text{int}}^{\text{av}}$ for $R = 20$ and 50 nm ($x_{\text{es}} = 0.2$ and 0.5) [Figs. 10(d) and 10(e)] appear to be similar, but the line shape for $R = 80$ nm ($x_{\text{es}} = 0.8$) [Fig. 10(f)] is considerably different; note the change in the scale of ordinate for Fig. 10(f) relative to that for Figs. 10(d) and 10(e). We obtained the spectra of $F_{\text{int}}^{\text{av}}$ by varying R with a step of 5 nm in the range $15 \text{ nm} \leq R \leq 80 \text{ nm}$ ($0.15 \leq x_{\text{es}} \leq 0.8$) and fitted to the generalized Fano function given by Eq. (14). The resulting fit curves for $R = 20, 50,$ and 80 nm ($x_{\text{es}} = 0.2, 0.5,$ and 0.8) are compared with the corresponding spectra of $F_{\text{int}}^{\text{av}}$ in Figs. 10(d), 10(e), and 10(f), respectively. The fit parameters obtained are plotted as a function of R in Figs. 11(a) to 11(d).

Figures 10(d) and 10(e) reveal that the $F_{\text{int}}^{\text{av}}$ spectra for $R = 20$ and 50 nm ($x_{\text{es}} = 0.2$ and 0.5) are well reproduced by the generalized Fano function. However, in Fig. 10(f) we see that the $F_{\text{int}}^{\text{av}}$ spectrum for $R = 80$ nm ($x_{\text{es}} = 0.8$) deviates considerably from the fit curve indicating that the line shape is deformed from the Fano line shape. Although it is difficult to set precisely an upper bound value R_{bound} for the validity of the generalized Fano function, we set it at $R_{\text{bound}} = 60$ nm ($x_{\text{es}} = 0.6$) from close comparisons between the spectra of $F_{\text{int}}^{\text{av}}$ and the fit curves. The fitting parameters plotted in Figs. 11(a) to 11(d) change monotonously depending on R and their deviations from the ES values increase as R increases. It should be noted that the R -dependencies of q and b for $F_{\text{int}}^{\text{av}}$ seen in Figs. 11(c) and 11(d) are quite different from those for F_{sca} seen in Figs. 5(c) and 5(d); in particular, the values of q are positive for $F_{\text{int}}^{\text{av}}$, while they are negative for F_{sca} .

We also examined the ϵ_m -dependence of the spectra for the model excitonic sphere of $R = 30$ nm. We calculated the spectra of FE^{av} , $FE^{\text{av}}_{\text{back}}$, and $F_{\text{int}}^{\text{av}}$ by varying ϵ_m with a step of 0.2 in a range $1.0 \leq \epsilon_m \leq 4.0$ ($0.3 \leq x_{\text{es}} \leq 0.6$). The spectra

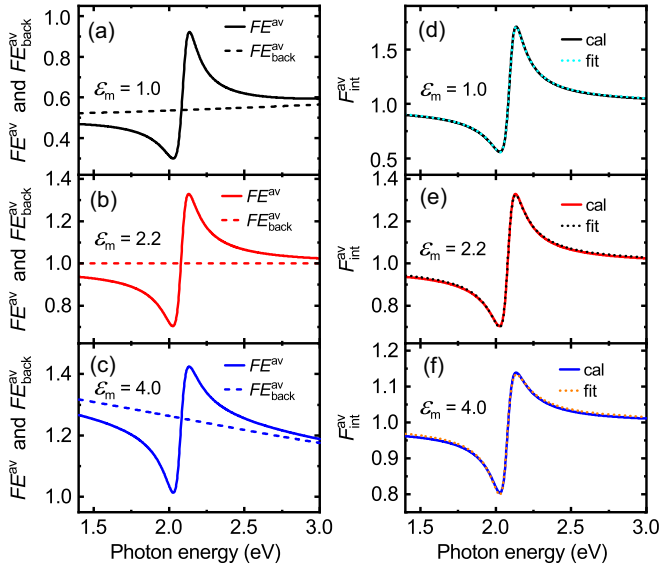


FIG. 12. Spectra of FE^{av} and $FE^{\text{av}}_{\text{back}}$ of the model sphere of $R = 30$ nm for (a) $\varepsilon_m = 1$ ($x_{\text{es}} = 0.3$), (b) $\varepsilon_m = 2.2$ ($=\varepsilon_b$) ($x_{\text{es}} = 0.4450$), and (c) $\varepsilon_m = 4.0$ ($x_{\text{es}} = 0.6$). In (d)–(f), corresponding spectra of $F_{\text{int}}^{\text{av}}$ are compared with curves resulting from the fitting to the generalized Fano functions [Eq. (14)].

of $F_{\text{int}}^{\text{av}}$ were again fitted to the generalized Fano function. The spectra of FE^{av} and $FE^{\text{av}}_{\text{back}}$ obtained for $\varepsilon_m = 1.0, 2.2$, and 4.0 ($x_{\text{es}} = 0.3, 0.4450$, and 0.6) are shown in Figs. 12(a), 12(b), and 12(c), respectively; the corresponding spectra of $F_{\text{int}}^{\text{av}}$ are compared with the fit curves in Figs. 12(d), 12(e), and 12(f). In Fig. 13, ε_m -dependencies of the fitting parameters are plotted; the solid lines in Fig. 13(c) and 13(d) show the behaviors of q [calculated by Eq. (35)] and b ($=1$) in the ES approximation. Figures 12(a), 12(b), and 12(c) show that the $FE^{\text{av}}_{\text{back}}$ spectrum, which is almost linear, changes its magnitude and slope depending on ε_m ; as ε_m increases, the overall magnitude increases, and the spectrum initially having a positive slope for $\varepsilon_m = 1.0$ turns to be flat at $\varepsilon_m = 2.2$ ($=\varepsilon_b$), and for further increase in ε_m , it takes a negative slope like that for

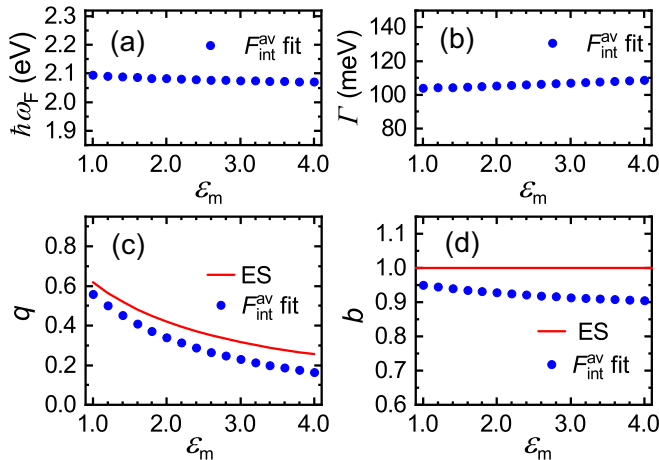


FIG. 13. ε_m -dependencies of the fitting parameters for the generalized Fano function. (a) ω_F , (b) Γ , (c) q , and (d) b . In (c) and (d), solid lines show behaviors in the small-particle limit.

$\varepsilon_m = 4.0$. Along with these changes in the $FE^{\text{av}}_{\text{back}}$ spectrum, the spectrum of FE^{av} also changes. However, the spectra of $F_{\text{int}}^{\text{av}}$ resulting from the factorization of FE^{av} by $FE^{\text{av}}_{\text{back}}$ are less sensitive to the change in ε_m as seen in Figs. 12(d), 12(e), and 12(f). Good agreements between the spectra of $F_{\text{int}}^{\text{av}}$ and fit curves seen in Figs. 12(d), 12(e), and 12(f) confirm that the generalized Fano function is capable of well describing the asymmetric line shape of $F_{\text{int}}^{\text{av}}$.

The above results of analytical analyses made in the small-particle limit and numerical calculations for the model excitonic sphere including the range of R beyond the small-particle limit indicate that the enhancement factor of the internal fields after the factorization to the background can be described by the generalized Fano function, exactly in the same manner as for the scattering spectra. However, we found quite different dependencies of the fit parameters q and b on R and ε_m , reflecting different characteristics of the internal and external Fano resonances. These differences can be attributed to the differences in the nominators of the Mie coefficients. In fact, as can be found in Eqs. (S3), (S4), (S9), and (S10) of the Supplemental Material [29], the denominators of a_n and d_n are identical as are those of b_n and c_n , but their nominators have different forms; the nominators of a_n and b_n become zero when $\varepsilon(\omega) = \varepsilon_m$, while those of d_n and c_n do not. Recall that a_n and b_n are the coefficients that connect the incident field to the scattered fields outside the sphere, which vanish when the dielectric constant of the sphere is identical to that of the surrounding medium. On the other hand, d_n and c_n connect the incident field to the local fields confined inside the sphere, which persist even when the scattered fields vanish. These differences in the coefficients lead to different characteristics of the external and internal Fano resonances.

IV. CONCLUSION

The spectra of scattering, absorption, and extinction efficiencies, Q_{sca} , Q_{abs} , and Q_{ext} , respectively, of a dielectric sphere that supports an excitonic transition were studied systematically based on the exact Mie theory and its ES approximation. Resonant behaviors of the enhancement factor of electric fields induced inside the sphere were also studied. The excitonic sphere is characterized by a dielectric function consisting of a background dielectric constant ε_b and a Lorentzian excitonic response. First, assuming a sphere much smaller than the wavelength of light (small-particle limit), line shape functions were derived analytically within the ES approximation. After factorizing the efficiencies by a background scattering efficiency Q_{back} , which describes the Rayleigh scattering in the small-particle limit, it was shown that the spectra of absorption are described by the Lorentzian function, while those of scattering and extinction are described by the generalized Fano function (external Fano resonance). Following the same procedures, it was also shown that the spectra of the internal field-enhancement factor can be described by the generalized Fano function (internal Fano resonance). The equations appearing in the derivations clearly indicate that the asymmetric line shapes in both the external and internal Fano resonances are generated by the interference between a nonresonant component corresponding to a broad background and a resonant component associated with the

excitonic transition. Analytical expressions obtained for the asymmetry parameter q of the Fano line shape and amplitude a of the Lorentzian line shape are useful for predicting the line shape changes caused by changes in the system parameters. In particular, we showed that the dependence of q and a on the dielectric constant of surrounding medium (ε_m) can generally be described as a function of $t = \varepsilon_m/\varepsilon_b$ by unified functions. For a model sphere, which mimics a polymer sphere doped with J-aggregates of excitonic molecules, it is shown that the spectra obtained within the ES approximation can be well reproduced by the line shape functions.

Based on the exact Mie theory, the calculation of the efficiency spectra as well as that of the internal field-enhancement factor was extended to the range of R beyond the small-particle limit. Although Q_{back} was found to deviate from that of Rayleigh scattering due to the contribution of higher-order electric and magnetic modes of the sphere, the Lorentzian and generalized Fano functions were shown to be still successful for reproducing the optical spectra, provided that R is smaller than a certain upper bound R_{bound} . The same conclusion could be drawn also for the internal Fano resonance. Even though both the external scattered fields and internal confined fields exhibit Fano-resonant behaviors, their dependencies on the system parameters were found to be quite different reflecting different characteristics of the Mie coefficients describing the external scattered fields and internal confined fields.

Although low-index dielectric nanoparticles not showing distinct Mie resonances have not attracted much attention so far, they can be good candidates of elements for resonant nanophotonics once the excitonic transition is incorporated. The Fano line shapes generated in their scattering and extinction spectra as well as in the spectra of internal fields can easily be controlled by the background dielectric constant and parameters of the excitonic transition. The present analytical and numerical results provide a firm basis for discussing the formation of the Fano line shapes in optical responses and spectra of internal fields of the excitonic sphere. Since the Rayleigh scattering or broad background scattering is a general characteristic of a small-enough particle or a particle with a small-enough background dielectric constant, irrespective of the particle shape, the conclusions drawn here for the spherical nanoparticle may be generalized to nanoparticles of arbitrary shape; further detailed studies in this direction are required.

ACKNOWLEDGMENTS

This work was supported by JSPS KAKENHI Grant No. 22K04967. This work was also partially supported by Kobe University Strategic International Collaborative Research Grant (Type B Fostering Joint Research).

-
- [1] A. E. Miroshnichenko, S. Flach, and Y. S. Kivshar, Fano resonances in nanoscale structures, *Rev. Mod. Phys.* **82**, 2257 (2010).
 - [2] B. Luk'yanchuk, N. I. Zheludev, S. A. Maier, N. J. Halas, P. Nordlander, H. Giessen, and C. T. Chong, The Fano resonance in plasmonic nanostructures and metamaterials, *Nat. Mater.* **9**, 707 (2010).
 - [3] M. F. Limonov, M. V. Rybin, A. N. Poddubny, and Y. S. Kivshar, Fano resonances in photonics, *Nat. Photon.* **11**, 543 (2017).
 - [4] M. F. Limonov, Fano resonance for applications, *Adv. Opt. Photon.* **13**, 703 (2021).
 - [5] G. Mie, Beitrage zur Optik trüber Medienspeziell Kolloidaler Metallösungen, *Ann. Phys.* **330**, 377 (1908).
 - [6] C. E. Bohren and D. R. Huffman, *Absorption and Scattering of Light by Small Particles* (John Wiley & Sons, New York, 1983).
 - [7] M. I. Tribelsky and B. S. Luk'yanchuk, Anomalous Light Scattering by Small Particles, *Phys. Rev. Lett.* **97**, 263902 (2006).
 - [8] M. I. Tribelsky, A. E. Miroshnichenko, and Y. S. Kivshar, Unconventional Fano resonances in light scattering by small particles, *Europhys. Lett.* **97**, 44005 (2012).
 - [9] B. Luk'yanchuk, R. Paniagua-Domínguez, A. I. Kuznetsov, A. E. Miroshnichenko, and Y. S. Kivshar, Suppression of scattering for small dielectric particles: Anapole mode and invisibility, *Phil. Trans. R. Soc. A* **375**, 20160069 (2017).
 - [10] M. I. Tribelsky, S. Flach, A. E. Miroshnichenko, A. V. Gorbach, and Y. S. Kivshar, Light Scattering by a Finite Obstacle and Fano Resonances, *Phys. Rev. Lett.* **100**, 043903 (2008).
 - [11] A. Miroshnichenko, Fano resonances in light scattering by finite obstacles, in *Fano Resonances in Optics and Microwaves*, Springer Series in Optical Sciences, Vol. 219, edited by E. Kamenetskii, A. Sadreev, and A. Miroshnichenko (Springer, New York, 2018), Chap. 20, p. 473.
 - [12] M. I. Tribelsky and A. E. Miroshnichenko, Giant in-particle field concentration and Fano resonances at light scattering by high-refractive-index particles, *Phys. Rev. A* **93**, 053837 (2016).
 - [13] K. Koshelev and Y. Kivshar, Dielectric resonant metaphotonics, *ACS Photon.* **8**, 102 (2020).
 - [14] H. Sugimoto and M. Fujii, Colloidal Mie resonators for all-dielectric metaoptics, *Adv. Photon. Res.* **2**, 2000111 (2021).
 - [15] Y. Kivshar, The rise of Mie-tronics, *Nano Lett.* **22**, 3513 (2022).
 - [16] H. Chen, L. Shao, Y. C. Man, C. Zhao, J. Wang, and B. Yang, Fano resonance in (gold core)-(dielectric shell) nanostructures without symmetry breaking, *Small* **8**, 1503 (2012).
 - [17] T. J. Arruda, A. S. Martinez, and F. A. Pinheiro, Unconventional Fano effect and off-resonance field enhancement in plasmonic coated spheres, *Phys. Rev. A* **87**, 043841 (2013).
 - [18] L. Jule, V. Mal'nev, T. Mesfin, B. Senbeta, F. Dejene, and K. Borro, Fano-like resonance and scattering in dielectric(core)-metal(shell) composites embedded in active host matrices, *Phys. Status Solidi B* **252**, 2707 (2015).
 - [19] Z. Wang, B. Luk'yanchuk, L. Yue, B. Yan, J. Monks, R. Dhama, O. V. Minin, I. V. Minin, S. Huang, and A. A. Fedyanin, High-order Fano resonances and giant magnetic fields in dielectric microspheres, *Sci. Rep.* **9**, 20293 (2019).

- [20] I. V. Minin, O. V. Minin, and S. Zhou, High-order Fano resonance in a mesoscale dielectric sphere with a low refractive index, *JETP Lett.* **116**, 144 (2022).
- [21] I. V. Minin, O. V. Minin, and B. S. Luk'yanchuk, Mesotronic era of dielectric photonics, *Proc. SPIE* **12152**, 121520D (2022).
- [22] B. S. Luk'yanchuk, A. R. Bekirov, Z. B. Wang, I. V. Minin, O. V. Minin, and A. A. Fedyanin, Optical phenomena in dielectric spheres several light wavelengths in size: A review, *Phys. Wave Phen.* **30**, 217 (2022).
- [23] F. Muckel, K. N. Guye, S. M. Gallagher, Y. Liu, and D. S. Ginger, Tuning hybrid exciton-photon Fano resonances in two-dimensional organic-inorganic perovskite thin films, *Nano Lett.* **21**, 6124 (2021).
- [24] E. Y. Tiguntseva, D. G. Baranov, A. P. Pushkarev, B. Munkhbat, F. Komissarenko, M. Franckevičius, A. A. Zakhidov, T. Shegai, Y. S. Kivshar, and S. V. Makarov, Tunable hybrid Fano resonances in halide perovskite nanoparticles, *Nano Lett.* **18**, 5522 (2018).
- [25] C. Cai, C. Bi, and T. Xu, Fano resonance in the CsPbBr₃ nanocrystal/Ag nanostructure through the exciton-plasmon coupling, *Appl. Phys. Lett.* **115**, 161602 (2019).
- [26] S. Makarov, A. Furasova, E. Tiguntseva, A. Hemmetter, A. Berestennikov, A. Pushkarev, A. Zakhidov, and Y. Kivshar, Halide-perovskite resonant nanophotonics, *Adv. Opt. Mater.* **7**, 1800784 (2019).
- [27] M. J. Gentile, S. Núñez Sánchez, and W. L. Barnes, Optical field-enhancement and subwavelength field-confinement using excitonic nanostructures, *Nano Lett.* **14**, 2339 (2014).
- [28] C. Tserkezis, P. A. D. Gonçalves, C. Wolff, F. Todisco, K. Busch, and N. A. Mortensen, Mie exciton: Understanding strong coupling in dielectric nanoparticles, *Phys. Rev. B* **98**, 155439 (2018).
- [29] See Supplemental Material at <http://link.aps.org/supplemental/10.1103/PhysRevB.108.125408> for a brief summary of basic equations of the Mie theory and its electrostatics approximation.
- [30] I. Avrutsky, R. Gibson, J. Sears, G. Khitrova, H. M. Gibbs, and J. Hendrickson, Linear systems approach to describing and classifying Fano resonances, *Phys. Rev. B* **87**, 125118 (2013).
- [31] D. V. Nesterenko, S. Hayashi, and Z. Sekkat, Asymmetric surface plasmon resonances revisited as Fano resonances, *Phys. Rev. B* **97**, 235437 (2018).
- [32] B. Gallinet and O. J. F. Martin, *Ab initio* theory of Fano resonances in plasmonic nanostructures and metamaterials, *Phys. Rev. B* **83**, 235427 (2011).
- [33] B. Gallinet and O. J. F. Martin, Influence of electromagnetic interactions on the line shape of plasmonic Fano resonances, *ACS Nano* **5**, 8999 (2011).
- [34] Z. Ruan and S. Fan, Temporal coupled-mode theory for Fano resonance in light scattering by a single obstacle, *J. Phys. Chem. C* **114**, 7324 (2010).
- [35] T. J. Arruda, R. Bachelard, J. Weiner, S. Slama, and P. W. Courteille, Fano resonances and fluorescence enhancement of a dipole emitter near a plasmonic nanoshell, *Phys. Rev. A* **96**, 043869 (2017).
- [36] H. Sugimoto and M. Fujii, Colloidal dispersion of subquarter micrometer silicon spheres for low-loss antenna in visible region, *Adv. Opt. Mater.* **5**, 1700332 (2017).
- [37] H. Sugimoto, T. Okazaki, and M. Fujii, Mie resonator color inks of monodispersed and perfectly spherical crystalline nanoparticles, *Adv. Opt. Mater.* **8**, 2000033 (2020).
- [38] D. Shima, H. Sugimoto, A. Assadillayev, S. Raza, and M. Fujii, Gallium phosphide nanoparticles for low-loss nanoantennas in visible range, *Adv. Opt. Mater.* **11**, 2203107 (2023).